Dynamic basis of lipopolysaccharide export by $LptB_2FGC$

Marina Dajka[1], Tobias Rath[2], Nina Morgner[2], & Benesh Joseph[1*]

[1]Department of Physics, Freie Universität Berlin, Arnimallee 14, 14195, Germany

[2]Institute of Physical and Theoretical Chemistry, Goethe Universität Frankfurt, Max-von Laue Strasse 9, 60438, Germany

[*]Corresponding author: benesh.joseph@fu-berlin.de

Abstract

Lipopolysaccharides (LPS) confer resistance against harsh conditions, including antibiotics, in Gram-negative bacteria. The lipopolysaccharide transport (Lpt) complex, consisting of seven proteins (A-G), exports LPS across the cellular envelope. $LptB_2FG$ forms an ATP-binding cassette transporter that transfers LPS to LptC. How $LptB_2FG$ couples ATP binding and hydrolysis with LPS transport to LptC remains unclear. We observed the conformational heterogeneity of $LptB_2FG$ and $LptB_2FGC$ in micelles and/or proteoliposomes using pulsed dipolar electron spin resonance spectroscopy. Additionally, we monitored LPS binding and release using laser-induced liquid bead ion desorption mass spectrometry. The β-jellyroll domain of LptF stably interacts with the LptG and LptC β-jellyrolls in both the apo and vanadate-trapped states. ATP binding at the cytoplasmic side is allosterically coupled to the selective opening of the periplasmic LptF β-jellyroll domain. In $LptB_2FG$, ATP binding closes the nucleotide binding domains, causing a collapse of the first lateral gate as observed in structures. However, the second lateral gate, which forms the putative entry site for LPS, exhibits a heterogeneous conformation. LptC binding limits the flexibility of this gate to two conformations, likely representing the helix of LptC as either released from or inserted into the transmembrane domains. Our results reveal the regulation of the LPS entry gate through the dynamic behavior of the LptC transmembrane helix, while its β-jellyroll domain is anchored in the periplasm. This, combined with long-range ATP-dependent allosteric gating of the LptF β-jellyroll domain, may ensure efficient and unidirectional transport of LPS across the periplasm.

Introduction

Antibiotic resistance poses a critical threat to global health, necessitating a comprehensive understanding of bacterial defence mechanisms. The outer membrane (OM), a crucial component of Gram-negative bacteria, serves as an initial line of defence against antibiotics[1]. Lipopolysaccharides (LPS) constitute a major component of the OM. LPS is a glycolipid consisting of lipid A, core oligosaccharides and an O-antigen[2]. The LPS transport (Lpt) system plays a central role in the biogenesis of OM, contributing significantly to its impermeability and resilience against environmental stress and host defenses[3-8]. The pathways for LPS synthesis, transport and regulation offers potential targets for novel antibiotics[9-13]. Comprising of seven essential components LptA-G (**Figure 1A**), the system orchestrates unidirectional translocation of LPS from the inner membrane (IM) to the OM[6,14]. The $LptB_2FG$ complex forms an ATP-binding cassette (ABC) transporter in the IM[4,15-17]. The LptB subunits constitute the nucleotide-binding domains (NBD)[18] and interact in a head-to-tail manner to create two nucleotide binding sites (NBSs, for ATP or ADP). The F and G subunits together form the transmembrane domains (TMDs) to create the LPS binding pocket[19-21]. The pseudo two-fold symmetry of the TMDs creates two lateral gates on either side of the TMDs. LptC connects LptF-LptG[20,22,23] with LptA[24] to transfer LPS through the trans-periplasmic bridge towards LptDE[25-28].

Previously, $LptB_2FG$ apo structures revealed open NBDs with bound LPS inside the TMDs (**Figure 1B-C**)[20,22,29]. Upon vanadate trapping, the NBDs dimerize causing a collapse of the LPS binding pocket, which has been suggested as a post-translocation state (**Figure 1D-E**)[20,23]. Presence of LptC enlarged the cavity leading to a weaker interaction with LPS (**Figure S1A-B**)[20,22,23]. In this conformation, the transmembrane (TM) helix of LptC weakly interacts with LptG, but forms extensive hydrophobic interactions with TM5 of LptF. The periplasmic β-jellyroll domains of LptF and LptG are very flexible leading to a reduced resolution. $LptB_2FGC$ structures in the AMP-PNP or vanadate-trapped state did not reveal the transmembrane helix of LptC (TM-LptC), thereby revealing a nearly identical conformation of NBDs and TMDs as with the $LptB_2FG$ structures[20,23]. Also, the β-jellyroll domains were barely resolved (**Figure S1C-D**).

It was proposed that upon ATP binding, TM-LptC moves away from the LptG-TM1 – LptF-TM5 interface. This would lead to a collapse of the binding pocket and expulsion of LPS to the β-jellyroll domain of LptF. However, several details of this mechanism such as when and how TM-LptC dissociates and in what way that is transmitted to the interaction and dynamics of the β-jellyroll domains remain poorly understood. Likely, many intermediate states might exist between ATP binding and LPS translocation and the relevance of the available structures in a native-like lipid environment is unknown. Altogether, an integrated characterization of the intermediate structures and underlying dynamics is required to elucidate the functional mechanism. Here we characterized the conformational heterogeneity of $LptB_2FG$ and $LptB_2FGC$ using extensive pulsed dipolar electron spin resonance (ESR) spectroscopy experiments, which permits observations in micelles, lipid bilayers or even in the native environments for certain cases [30-41]. These observations were further correlated with results obtained using laser-induced liquid bead ion desorption mass spectrometry (LILBID-MS)[42,43]. Our results provide novel insights into the allosteric regulation of the structure and dynamics of the TMDs and the β-jellyroll domains during ATP binding and hydrolysis, which altogether drive LPS translocation.

Results

Conformational heterogeneity of $LptB_2FG$ in micelles and liposomes

Initially, we characterized the dynamics of $LptB_2FG$ in both DDM micelles and proteoliposomes (PLS) using pulsed electron-electron double resonance (PELDOR or DEER) spectroscopy[44,45]. This technique has been used for investigating several Type I, type II, type III and type IV ABC transporters [31,38,46-52]. $LptB_2FG$ belongs to the type VI class of ABC transporter. For this purpose, we engineered spin pairs along the NBDs, TMDs and the β-jellyroll domains (**Figure 2-6, Figure S2**). Following reaction with a cysteine, the (1-Oxyl-2,2,5,5-tetramethyl-3-pyrroline-3-methyl)methanethiosulfonate (MTSL)) label creates the side chain denoted as R1[53]. The functionality of all the spin labelled variants after size -exclusion chromatography was confirmed

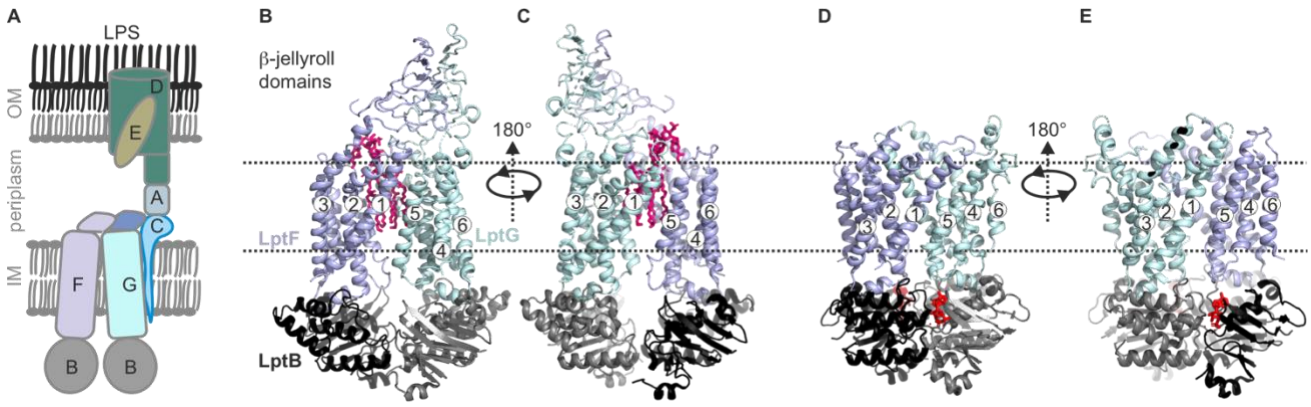

Figure 1. Lipopolysaccharide transport (Lpt) system. (A) the Lpt system consists of the $LptB_2FG$-C complex located in the inner membrane (IM). Periplasmic LptA connects this complex with LptDE, which is located in the outer membrane (OM). (B, C) Structures of $LptB_2FG$ in the LPS-bound state (PDB ID: 6MHU) or (D, E) in the vanadate-trapped state (PDB ID: 6MHZ) are shown. In the vanadate-trapped structure, the cavity is collapsed with no space for LPS and the β-jellyroll domains are not resolved. The LPS molecule (magenta) and nucleotides (red) are highlighted.

using ATP-ase activity assay (**Figure S3-S4**). All the cysteine variants could be labelled with high efficiency (**Figure S5 and Table S1**). We investigated $LptB_2FG$ under several conditions including the apo-state or after incubating with ATP-EDTA (EDTA to chelate divalent metal ions and to inhibit any residual ATPase activity), ATP-Mg^{2+}-VO_4^{3-} (vanadate-trapped transition state) or ADP-Mg^{2+} (post-hydrolysis state).

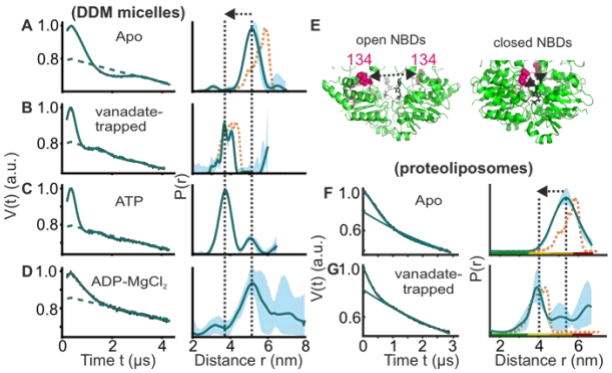

Figure 2. DEER/PELDOR data for the NBDs of $LptB_2FG$ in micelles and PLS. (A-E, H-J) Primary data overlaid with the fits obtained using the DeerLab[54] program (A-E in micelles) or ComparitiveDeerAnalyzer[54,55] (H-J in PLS) are shown in the left panels. The obtained distance distributions with a 95% confidence interval are shown on the right. Simulations for the open (PDB ID: 6MHU) or closed (PDB ID: 6MHZ) structures are overlaid with the apo or vanadate-trapped distances, respectively (in dotted orange line). (F, G) The spin labelled positions (as sphere) and the loops carrying them are highlighted (in red) on the open and closed structures. The PLS samples were analysed using ComparitiveDeerAnalyzer to account for the entire uncertainty including the partial dimensionality for spin distribution over the membrane surface.

In agreement with the apo structure, the NBDs displayed a mean interspin distance centred around 5 nm in micelles when observed at position B_M134R1 (**Figure 2A-D**). This distance decreased below 4 nm in the vanadate-trapped state. With ATP(EDTA) a mixed population was observed with the major peak corresponding to the closed conformation. Thus, Mg^{2+} ions are not necessary for the closure of the NBDs. With ADP-Mg^{2+} the NBDs do not close, though the overall flexibility is somewhat increased (as gauged from the width of the distribution). We performed additional experiments after reconstitution into PLS (**Figure 2F-G**). Overall, the data in the apo-state revealed a similar mean distance, yet with a larger width suggesting an increased dynamics. As observed in micelles, vanadate-trapping closed the NBDs in PLS as well. Overall, the ATP-induced closure as observed in micelles (and the structures) is maintained in the native-like lipid bilayers for the NBDs.

Conformational heterogeneity of the lateral gates of $LptB_2FG$ in micelles and PLS

We introduced two spin pairs to independently monitor the lateral gates of the TMDs. The lateral gate formed by LptF-TM1 – LptG-TM5 and LptG-TM1 – LptF-TM5 were monitored using F-A45R1_G-I325R1 and F-L325R1_G-A52R1 pairs, respectively. For the apo-sate in micelles, the distances for the lateral gate-1 are similar to the corresponding simulation on the LPS-bound structure (**Figure 3A**). Vanadate-trapping resulted in an increase of the distances in agreement with the simulation. Though the central cavity collapses, this increased distance results from a coordinated movement of LptF-TM1 towards the cavity accompanied with an outward shift of LptG-TM5 (**Figure 3E and Figure S1-S2**). Addition of ATP(EDTA) resulted in an equilibrium between the two conformations. Altogether, the PELDOR data validate a LPS binding competent conformation in the apo- and ADP-Mg^{2+} states accompanied with a collapse of the gate in the ATP and vanadate-trapped post-hydrolytic state. Interestingly, for the apo state in PLS, this gate exhibited a broader distribution spanning the range corresponding to both structures (**Figure 3F-G**). In the vanadate-trapped state the overall distribution got narrowed (the minor peak at a longer distance is not interpreted due to a larger uncertainty). However, the overall spread of the distribution remained similar, suggesting a more flexible conformation of this gate in PLS, which is minimally affected by ATP binding.

The putative lateral gate for LPS entry exhibits a large conformational heterogeneity

Interestingly, the lateral gate-2 between LptG-TM1 – LptF-TM5 revealed a more dynamic behaviour in micelles (**Figure 4A-D**). In the apo state, it has a broad conformational distribution spanning the LPS bound (open) and vanadate-trapped (closed) structures (corresponding simulations are shown in orange lines). In the vanadate-trapped and ATP samples, the major population is centred at 2 nm (which corresponds to the simulation on the vanadate-trapped structure). The decreased interspin distances arise from a collapse of the cavity upon vanadate-trapping (**Figure 4E and Figure S1-S2**). Unlike the lateral gate-1 (and the NBDs), ADP-Mg^{2+} also induced a similar shift in the distance distribution. Why ADP-Mg^{2+} induce a change for this gate (alone) calls for further investigation. An asymmetric interaction of the cytoplasmic loop2 (linking TM4 and TM5 in both LptF and LptG), which was shown to interact with nucleotides[20] could have a role here. In PLS as well, the apo state revealed a broad distribution validating the

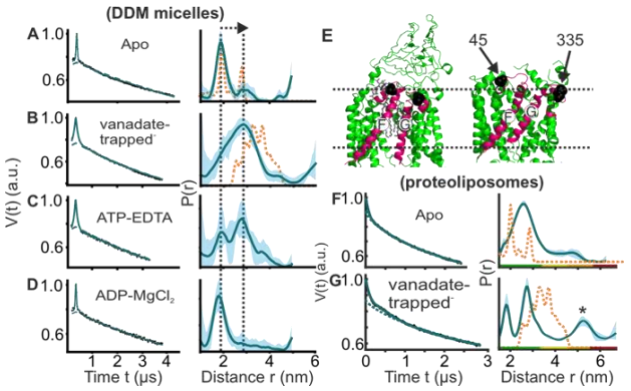

Figure 3. DEER/PELDOR data for the lateral gate-1 between LptF-TM1 – LptG-TM5 of LptB$_2$FG in micelles and PLS. (A-E, G-I) Primary data overlaid with the fits obtained using the DeerLab program (A-E in micelles) or ComparitiveDeerAnalyzer (G-I in PLS) are shown in the left panels. The obtained distance distributions with a 95% confidence interval are shown on the right. (F) The spin labelled positions are highlighted on the open (PDB ID: 6MHU) and closed (PDB ID: 6MHZ) structures and the corresponding simulations are overlaid with the apo or vanadate-trapped distances, respectively (in dotted orange line). The distance peak indicated with an asterisk in H is not interpreted for the reason of a larger uncertainty.

heterogeneity in the membrane environment (**Figure 4F-G**). Vanadate-trapping somewhat narrowed the distribution with (only) a fraction of the distances overlaying with the simulation for the corresponding structure (with a more pronounced heterogeneity as compared with the micellar sample, **Figure 4B**). Position L325 investigated here is located on short loop between TM5 and TM6 in LptF. This loop is resolved with clear density and has a similar orientation in the apo and vanadate-trapped structures with minimum deviation (**Figure 4E, S6**). Also, the experimental data in the vanadate trapped state is in agreement with the shift of the helices as observed from the structure (**Figure 4B, E and Figure S1-S2**). Therefore, the internal flexibility of this short loop might have the least contribution to the broad distribution we experimentally observed. Comparing this heterogeneity from the PELDOR data (**Figure 4**) with the corresponding simulations (in orange, **Figure 4A-B**), it appears that the structures captured two of the states from the broad conformational space. This gate is suggested to be the entry point for LPS[22] and the enhanced dynamics we observed might be required for efficient interaction with LPS and LptC (please see later sections). Supporting these observations, LptG-TM1 and LptF-TM5 helices interact rather weak in the structures, in particular in the LPS-bound state (**Figure 1C, E and Figure S1-S2**).

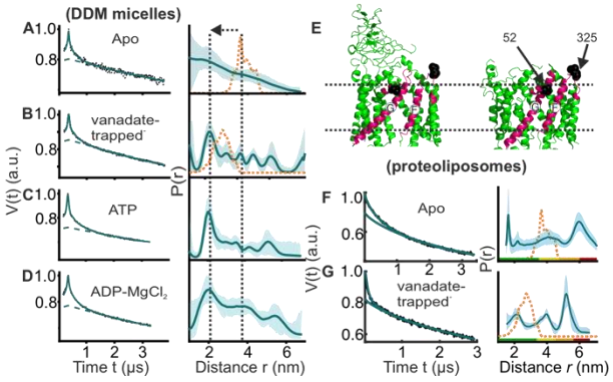

Figure 4. DEER/PELDOR data for the lateral gate-2 between LptF-TM5 – LptG-TM1 of LptB$_2$FG in micelles and PLS. (A-E, G-I) Primary data overlaid with the fits obtained using the DeerLab program (A-E in micelles) and ComparitiveDeerAnalyzer (H) or DeerNet (G, I) in PLS are shown in the left panels. The obtained distance distributions with a 95%confidence interval are shown on the right. Due to a larger uncertainty arising from the broad distribution and the limited time-window, output from DeerNet is shown in G and I. (F) The spin labelled positions are highlighted on the open and closed structures. Simulations for the open (PDB ID: 6MHU) or closed (PDB ID: 6MHZ) structures are overlaid with the apo or vanadate-trapped distances, respectively (in dotted orange line).

Conformational dynamics of the β-jellyroll domains

We further investigated the interaction between the β-jellyroll domains in LptB$_2$FG. Distances between positions F-S186R1 and G-V209R1 located on these domains revealed a major peak in agreement with simulation on the LPS-bound structure (**Figure 5A-B**) and a previous study[56] employing isolated β-jellyroll domains. The overall spread of the distribution remained rather similar in the vanadate-trapped state

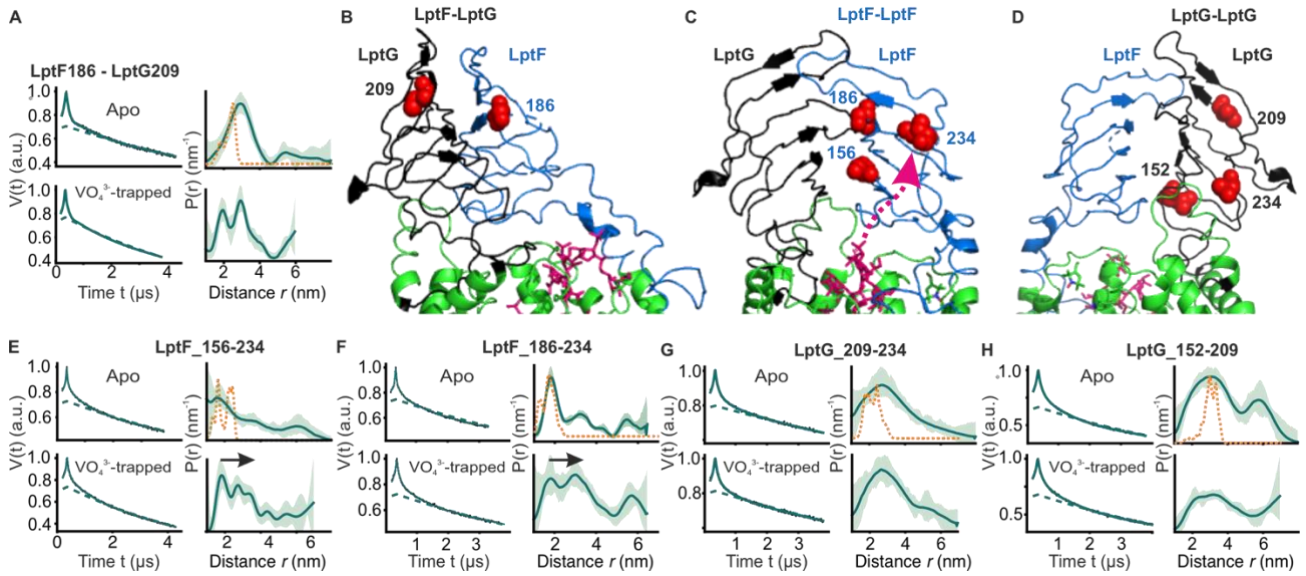

Figure 5. DEER/PELDOR data for β-jellyroll domains of LptB$_2$FG. (A) Primary data for LptF-LptG β-jellyrolls overlaid with the fits obtained using the DeerLab[54] program are shown in the left panels. The obtained distance distributions with a 95% confidence interval are shown on the right. (B-D) The spin labelled positions are highlighted on the LptB$_2$FG apo structure and the bound LPS is shown in stick representation (PDB ID: 6MHU). (E, F) Primary data overlaid with the fits and the corresponding distance distributions (right) from PELDOR experiments within the β-jellyroll domain of LptF or LptG (G, H). Corresponding simulations (where structures are available having the positions resolved) are overlaid (in orange).

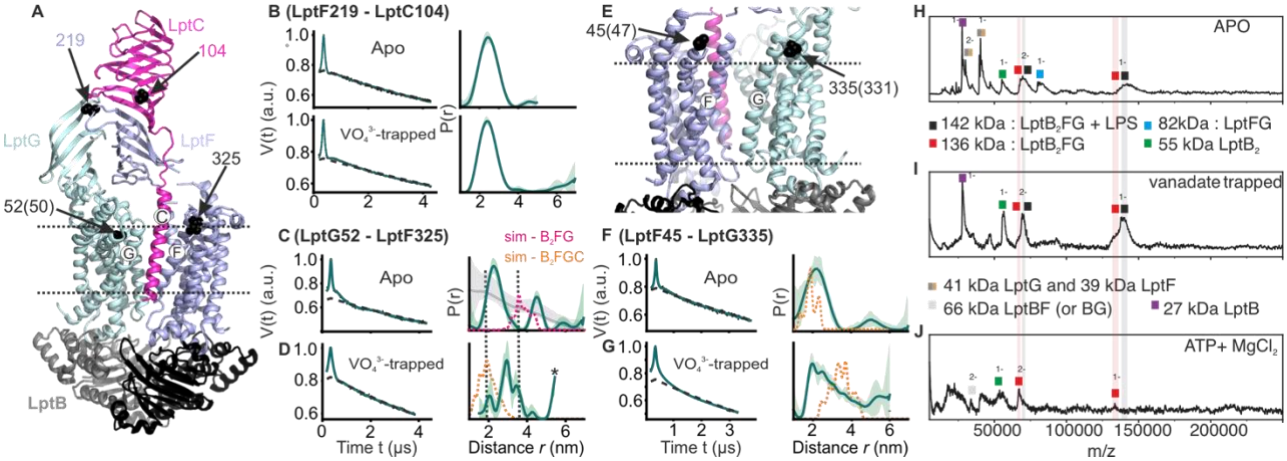

Figure 6. DEER/PELDOR data for the lateral gates of LptB$_2$FGC and LILBID-MS. (A) The LptB$_2$FGC structure (PDB ID: 6MJP) from *Vibrio cholerae*. The helices from LptF and LptG forming the lateral gate-2 is shown and the positions analogous to those we investigated in the *E. coli* structure are highlighted (in sphere representation, when the amino acid number is different, it is indicated inside the bracket). (B-D, F) Primary PELDOR data overlaid with the fits obtained using the DeerLab[54] are shown in the left panels. The obtained distance distributions with a 95% confidence interval are shown on the right. Asterisk on the bottom-right in panel (C) indicate unreliable distances and the corresponding distances for LptB$_2$G is overlaid for a comparison (in grey for the apo state). Simulation on the LptB$_2$FGC apo structure (in orange) is overlaid in panel (F). In panel C, corresponding distances for LptB$_2$FG is overlaid (in grey) and the simulation for LptB$_2$FG structure is shown (in magenta) as position L325 is not resolved in the *E. coli* LptB$_2$FGC structure. (H-J) LILBID-MS data for detergent solubilized LptB$_2$FG in different states as indicated.

revealing a stable interaction. We also probed the internal flexibility of LptF β-jellyroll using F_S156R1– I234R1 and F_S186R1 – I234R1 pairs, which are located on the putative entry gate loops for LPS[22] (**Figure 5C, E-F**). The LptF β-jellyroll in the apo-state showed a broad distribution, but with a major population staying in the closed conformation as observed in the structure (**Figure 5E, F**). Interestingly, in the vanadate-trapped state, the overall distribution shifted towards longer distances revealing an opening of the LPS entry gate. Altogether, these observations reveal a long-range allosteric coupling between nucleotide binding at the NBDs in the cytoplasm and opening of the LPS entry gate of LptF β-jellyroll in the periplasm. Such a tight coupling might prime this domain to receive LPS once it is released from the cavity inside the TMDs. A strikingly different response was observed for the β-jellyroll domain of LptG. The equivalent spin pairs G_V209R1 – G_L234R1 and G_L152R1 – V209R1 revealed a considerably enhanced flexibility independent of ATP (**Figure 5D, G-H**) and revealing no such allosteric coupling with the NBDs.

Conformational heterogeneity of LptB$_2$FGC

Next, we investigated how LptC modulates dynamics of the lateral gates and the β-jellyroll domains in LptB$_2$FG. Measurements between the β-jellyroll domains of LptF and LptC (F_L219R1 – C_T104R1) revealed a narrow distance distribution and hence a stable interaction between them in both apo and vanadate-trapped states (**Figure 6A-B**). At the lateral gate-1 (F_A45R1-G_I335R1, **Figure 6E** and **F-G**), the distance in the apo state is similar to the simulation on the structure. In the vanadate trapped state, the spread of the distance distribution is increased, spanning the range of the simulations corresponding to both apo and vanadate-trapped structures (in the latter structure, TM-LptC is absent at the gate leading to a collapse of the cavity and an identical conformation with LptB$_2$FG, though the distances increase due to an outward movement of LptG-TM5, see **Figure 3B,E and Figures S1-S2**). Distances corresponding to the apo state are present possibly due to an incomplete vanadate-trapping (or an equilibrium between the two conformations, which is rather unlikely) for this sample. Overall, the results support TM-LptC dissociation in the vanadate-trapped state as observed in the structure.

A distinct response is observed for the lateral gate-2 (F_L325R1 – G_A52R1, **Figure 6A** and **C-D**). LptC binding reduced the overall flexibility of this gate into two defined distance peaks as compared to LptB$_2$FG alone (**Figure 4A vs.6C**). LptC binding is shown to increase the separation between these helices (**Figure S1A**). The major distance peak (centred around 2 nm) is shorter than the simulation on the LptB$_2$FG apo structure (in magenta, **Figure 6C**, top panel), which therefore likely represents a conformation in which TM-LptC is released. The second peak corresponds to a larger separation between these helices, possibly representing the structure having the TM-LptC inserted at the gate (as position L325 is not resolved in the *E. coli* structure, corresponding simulation is not presented). The first conformation appears to be more favoured under the experimental conditions. In the vanadate-trapped state, the second peak disappeared and the overall distribution centred towards the TM-LptC released (LptB$_2$FG) conformation (**Figure 6D**). This is in line with the lack of density for TM-LptC in the vanadate-trapped LptB$_2$FGC structure. The experimental distribution is longer than the corresponding simulation (**orange line in Figure 6D**), suggesting a somewhat farther separation between these helices.

We further probed LPS release in LptB$_2$FG using LILBID-MS (**Figure 6H-J**). In the apo and vanadate-trapped states, the majority of the observed complex peaks represent LPS bound to LptB$_2$FG, while some LPS free LptB$_2$FG can as well be seen (indicated in grey and red shades, respectively for both 1- and 2- charge states). Presence of LPS-bound LptB$_2$FG in the vanadate-trapped state is not unexpected as the PELDOR data revealed a heterogenous conformation for the LPS entry gate other than the collapsed conformation (**Figure 4B and H**). However, under the hydrolysing conditions, LPS is completely released from LptB$_2$FG.

Discussion

LPS transport by LptB$_2$FG remained elusive for many reasonsLptB$_2$FG and LptB$_2$FGC structures revealed a similar structure in the vanadate-trapped state leaving no trace for the TM-LptC and the β-jellyroll domains (**Figure S1D**). Available structures possess either AMP-PNP or ADP-VO4^{3-} as nucleotides (both in a closed conformation of the TMDs and NBDs), thereby limiting details on how ATP binding and

hydrolysis are coupled to the conformational changes and LPS transport.

For the NBDs and the two lateral gates of $LptB_2FG$, PELDOR data validated the conformational changes in micelles as observed from the structures. Upon ATP binding and/or vanadate-trapping, the NBDs and the two lateral gates moved in a coordinated manner to collapse the LPS binding pocket (**Figures 2-4**). However, the lateral gate-2 forming the LPS entry site (TM1G -TM5F monitored by F_L325 – G_A52, **Figure 4, S1 and S2**) exhibits a very flexible conformation (even with nucleotides), which might facilitate interaction with LPS and or LptC. In agreement, LptC binding restricted the overall flexibility of this gate into two distinct conformations corresponding to a collapsed and an open conformation in which TM-LptC is likely inserted into the TMDs (**Figure 6C,** top panel). The minor peak at longer distances might corresponds to a conformation in which TM-LptC and LPS can enter the TMDs while the β-jellyroll domains of LptC and LptF interact. (**Figure 6B**). The minimal interaction between the corresponding helices (**Figure S1-S2**) in the $LptB_2FG$ structures suggest that the flexibility is inbuilt and might have an important role for the function. The PLS environment modulates the observed conformation in $LptB_2FG$. The lateral gate-1 has a broader distribution in PLS, which is minimally affected by vanadate-trapping (**Figure 3F-G**). Also, the heterogeneity for the lateral gate-2 is more pronounced in PLS. Yet, the observations are qualitatively similar to the micellar sample (also see **Figure S7** for the continuous wave (cw) ESR spectra) and further experiments are required to clarify how the membrane would influence $LptB_2FGC$ conformation.

In $LptB_2FG$, the two β-jellyroll domains stably interact in the apo and vanadate-trapped conditions (**Figure 5**). Interestingly, binding of nucleotides is allosterically coupled to a selective opening of LptF β-jellyroll with little effect on the LptG β-jellyroll (**Figure 5E-H**). This opening was shown to be essential for cell growth and it was suggested that movement of LPS, but not ATP binding or hydrolysis pushes the gate open[22]. However, our results confirm that the gate opening is allosterically regulated through ATP binding and/or hydrolysis. This β-jellyroll start from TM3 and ends on TM4. TM3 is connected to the coupling helix and TM4 is connected to the cytoplasmic loop-2, which harbours the conserved R292 directly interacting with the nucleotide[20]. It is likely that one or both of these motifs are involved in the allosteric communication. Notably, the LptG β-jellyroll domain exhibits significant internal flexibility (**Figure 5G-H**). Biochemical studies showed that conserved residues in this domain are essential for cell growth[20]. Though there is little evidence for a direct role of this domain in LPS binding, the observed dynamics might be important for efficient transport. Similarly, in $LptB_2FG$-C, the β-jellyrolls of LptC and LptF interact both in both apo and vanadate-trapped states (**Figure 6A-B**), which altogether might form a continuous pathway for LPS transfer towards LptA. The β-jellyrolls were not fully resolved in the vanadate-trapped structure of $LptB_2FG$ (**Figure 1**) and $LptB_2FGC$[23], revealing a considerable flexibility. The exact role for this enhanced dynamics is unclear and it may somehow facilitate LPS release. The narrow distance distributions we observed reveal that these domains might move as rigid bodies while sampling a broad conformational space.

The LILBID-MS data show that LPS is released upon ATP hydrolysis by $LptB_2FG$ (**Figure 6H-J, Figure 7 steps 1-2**). Thus, LptC is required for a productive transport cycle in the wild-type protein[24,57,58]. Our observations suggest that the TM-LptC dynamically associates and dissociates at the lateral gate-2, even in the apo-state while its β-jellyroll domain is firmly bound to LptF β-jellyroll (**Figure 7, step 3**). Such a dynamic behaviour of TM-LptC has previously been suggested based on the *Klebsiella pneumoniae* $LptB_2FGC$ structure, which showed density for the short N-terminus

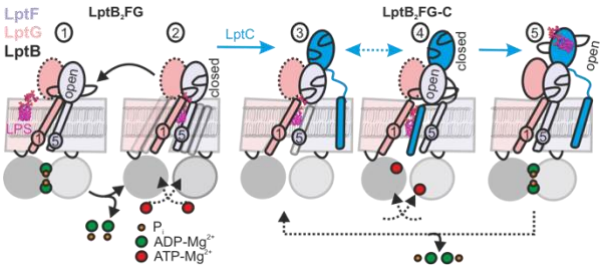

Figure 7. LPS translocation mechanism. (1-2) The lateral gate-2 formed by LptG-TM1 and LptF-TM5 in $LptB_2FG$, which is very dynamic in the apo state (2) is shown (**see Figure 4**). ATP binding, which leads to hydrolysis (1) collapses the cavity and releases LPS. (3,4) Interaction with LptC limits heterogeneity, creating an equilibrium between TM-LptC inserted and released conformations (**Figure 6C**). ATP binding opens the periplasmic gate in LptF β-jellyroll (4) and subsequent closure of the NBDs leads to the collapse of the cavity and LPS transfer. As LPS moves to LptC, LptF β-jellyroll might close accompanied with an opening of LptC β-jellyroll[20] (5). Dissociation of ADP-Mg^{2+} will initiate the next cycle according to the Pez mechanism. Dotted line for LptG β-jellyroll indicates enhanced inter-domain dynamics (**see Figure 5G-H**).

segment of TM-LptC[59]. Vanadate trapping induces the TM-LptC released conformation of the lateral gates (**Figure 6C-D and F-G**), in agreement with the structures, which also leads to LPS release[20,22]. Thus, ATP binding/hydrolysis might be coupled to the collapse of the TMDs and expulsion of LPS. Inferring from our observations on $LptB_2FG$ (**Figure 5**), ATP binding might allosterically open the LptF β-jellyroll (**Figure 7, step 4**), which might subsequently close after passing LPS to the LptC β-jellyroll to prevent any backflow[20] (**Figure 7, step 5**). Through repeating this cycle, $LptB_2FG$ might push LPS along the trans- periplasmic bridge in a unidirectional manner according to the Pez candy dispenser model[60]. The possibility to observe $LptB_2FG$ and $LptB_2FGC$ offers further opportunity to characterize the dynamics of the β-jellyroll domains, $LptB_2FG$ – TM-LptC interaction as well as other intermediate states of the transport cycle even in the native-like lipid bilayers. These experiments, which are beyond the current scope of the study are in progress in our laboratory. As the persistently interacting, yet dynamic $LptB_2FGC$ complex forms the functional LPS transport unit in the inner membrane, a detailed understanding of its dynamics would facilitate development of novel drugs against Gram-negative bacterial pathogens.

Materials and Methods

Expression, purification and spin labeling of $LptB_2FG$ and $LptB_2FG$-C

The plasmid pETDuet-*lptB-lptFG*, including a C-terminal His-tag on LptB, was used to transform in *E. coli* BL21(DE3) C43 for $LptB_2FG$ expression. For $LptB_2FGC$ a co-expression with the pCDFDuet-1-*lptC* together with pETDuet-*lptB-lptFG* was performed. For bacterial cell growth Luria broth (LB) medium with 100 µg/mL ampicillin (for $LptB_2FG$, and additionally 50µg/mL streptomycin for $LptB_2FGC$) was incubated at 37 °C until an optical density of 1.0 at 600 nm. The protein expression was induced with 0.2 mM or 0.4 mM isopropyl β-D-1-thiogalactopyranoside (IPTG) for $LptB_2FG$ and $LptB_2FGC$, respectively. After overnight expression at 18 °C the cells were collected by centrifugation. Cell pellets were resuspended in lysis buffer (20 mM HEPES, pH 7.5, 300 mM NaCl) with a homogenizer and lysed by French press with an additional spatula tip of DNAse I, lysozyme and 100 µg/ml PMSF. Cell debris was removed by centrifugation at 12,000xg for 20 min at 4 °C. The membranes were

pelleted by ultra-centrifugation at 200,000xg for 2 h at 4 °C. Membranes were flash-frozen in liquid nitrogen and stored at -80 °C. For solubilization lysis buffer with 1% (w/v) DDM was used and after homogenization membranes were incubated for 30 min at 4 °C. The protein solution was ultra-centrifugated at 100,000xg for 35 min at 4°C. The supernatant was incubated with washed Ni Sepharose (High Performance, GE Healthcare) for 45 min at 4 °C and loaded on an empty PD-10 column (GE Healthcare). The column was washed with 15 column volumes of wash buffer containing 20 mM HEPES, pH 7.5, 300 mM NaCl, 0.05% (w/v) DDM, 5% (v/v) glycerol and 40 mM imidazol. The protein bound to the Ni Sepharose was labeled with 2 column volumes of 20 mM HEPES, pH 7.5, 300 mM NaCl, 0.05% (w/v) DDM, 5% (v/v) glycerol and 300 µM MTSL (1-Oxyl-2,2,5,5-tetramethyl-3-pyrroline-3-methyl)methanethiosulfonate for 1.5 h at 4°C. The column was washed with 40 column volumes of the same buffer (without MTSL) and further eluted with 300 mM imidazole and immediately deslated using a PD-10 desalting column (GE Healthcare) into the same buffer. The protein was then concentrated to about 100 µM (Amicon Ultra-15, PLQK Ultracel-PL Membrane, 50 kDa, Merck, Millipore). After size-exclusion chromatography with a Superdex 200 Increase10/300 GL column (GE Healthcare), the protein fractions were collected and concentrated to ~40 µM protein. For PELDOR spectroscopy different samples were prepared. For the ATP-EDTA sample, 5 mM ATP and 0.5 mM EDTA were added (5 min, 37 °C). The ADP-$MgCl_2$ sample contained 5 mM ADP and 5 mM $MgCl_2$ (1 min, RT). The vanadate-trapped sample was prepared with 5 mM ATP, 5 mM $MgCl_2$ and 5 mM *ortho*-vanadate and the sample was incubated for 5-10 minutes at 37°C. All the samples were adjusted to the same final protein and DDM concentration (0.05%).

Proteoliposome reconstitution and PELDOR sample preparation

Liposomes (20 mg/mL, 20 mM HEPES, 300 mM NaCl, 10% (v/v) glycerol, pH 7.5) were mixed with 0.14% Triton-X and incubated for 30 min at room temperature. Liposomes and protein (in the same buffer additionally containing 5% glycerol and 0,05% (w/v) DDM) were mixed at 1:10 (w/w) ratio to a final lipid concentration of 4 mg/mL in 10 mL. The protein-lipid suspension was gently incubated for 1 h at room temperature. Afterwards Bio-Beads SM-2 (Bio-Rad) was added and was gently mixed for 30 min at room temperature and moved to 4º C. The Bio-Beads were added three more times for the following incubation periods at 4ºC: 1 h, overnight and 2 h. Proteoliposomes were diluted to 2 % (v/v) glycerol in 20 mM HEPES, 300 mM NaCl, pH 7.5 and were pelleted at 200,000xg (4 °C) and resuspended into the same buffer. PELDOR samples were prepared as described above for DDM micelles with an additional freeze-thaw (5x) cycle. Samples were frozen in liquid nitrogen and stored at -80 ºC.

ATP assay

The ATP assay was performed according to a protocol modified from Morbach *et al*[61]. 5 µg of purified $LptB_2FG$ or $LptB_2FGC$ were incubated at 37 °C for 8 min in 25 µL reaction volume on a 96-well plate with different ATP concentrations (0, 0.125, 0.25, 0.5, 1, 2, 3 and 5 mM) in 20 mM HEPES pH 7.5, 150 mM NaCl, 0.05 % (w/v) DDM and 5 mM $MgCl_2$. The reaction was stopped with addition of 150 µL of 20 mM H_2SO_4. A 50 µL working solution [50 ml of ddH_2O, 10 ml of ≥ 95 % H_2SO_4 and 73.4 mg of malachite green chloride, 40 µl of 11 % Tween 20, and 500 of µl 7.5 % (w/v) $(NH_4)_6Mo_7O_{24}.4H_2O$ solution] was added and incubated for 8 min at RT and the absorbance was measured at 620 nm in a microplate reader. The data was analyzed using Origin 2018.

Continuous wave (cw) ESR spectroscopy

Continuous wave ESR spectroscopy measurements were performed on a X-band Bruker EMXnano benchtop spectrometer. A 16 µL of the protein sample was measured in a 0.64 mm diameter micropipette (BRAND, Germany) with 100 kHz modulation frequency, 0.6-2 mW microwave power, 0.15 mT modulation amplitude and 18 mT sweep width.

Pulsed electron-electron double resonance spectroscopy

DEER/PELDOR experiments were conducted on a Bruker Elexsys E580 Q-Band (34 GHz) pulsed ESR spectrometer equipped with an arbitrary waveform generator (SpinJet AWG, Bruker), a 50 W solid-state amplifier, a continuous-flow helium cryostat, and a temperature control system (Oxford Instruments). Measurements were carried out at 50 K using a 10 – 20 µL frozen sample containing 15 – 20% glycerol-d_8 in a 1.6 mm quartz ESR tube (Suprasil, Wilmad LabGlass) with a Bruker EN5107D2 dielectric resonator. The phase memory time (T_M) measurements were performed with a 48 ns $\pi/2-\tau-\pi$ Gaussian pulse sequence with a two-step phase cycling after incrementing τ in 4 ns steps. A dead-time free four-pulse sequence with a 16-step phase cycling ($x[x][x_p]x$) was used for DEER measurements[62]. A 38 ns Gaussian pump pulse (with a full width at half maximum (FWHM) of 16.1 ns) was employed, along with a 48 ns observer pulse (FWHM of 20.4 ns)[63]. The pump pulse was placed at the maximum of the echo-detected field swept spectrum, and the observer pulses were set 80 MHz lower. Deuterium modulations were averaged by progressively increasing the first interpulse delay by 16 ns over 8 steps. The data analysis was performed with the ComparativeDeerAnalyzer 2.0 (CDA)[54,55] or the DeerLab program. The distance distributions were simulated on the structures (PDB 6MHU, 6MHX, 6MI7 and 6MI8) using a rotamer library approach as implemented in the MATLAB-based MMM2022.2 software package[64].

Liquid bead ion desorption mass spectrometry (LILBID-MS)

For analysis by LILBID-MS, samples were buffer exchanged to 20 mM Tris(HCl), 0.05% DDM, pH 7.5. For ATP-Mg^{2+} sample, 2 mM ATP and 0.5 mM $MgCl_2$ were added prior to the buffer exchange and the sample was incubated for 1 min at room temperature. After dilution to 10 µM protein, 4 µL of the sample were loaded directly into a droplet generator (MD-K-130, Microdrop Technologies GmbH, Germany). This piezo driven device generates droplets of a diameter of around 50 µm at a frequency of 10 Hz. The droplets are then transferred into vacuum, and irradiated by an IR laser working at a wavelength of 2.8 µm having a maximum energy output of 23 mJ per pulse (6 ns). The free ions were accelerated into a homebuilt time of flight analyser by applying an acceleration voltage in the Wiley McLaren type ion optics. The voltage between the first and the second lens was set to -4.0 kV. At 5 to 25 µs after irradiation, the first lens was pulsed to -6.6 kV for 370 µs, while the reflectron worked at -7.2 kV. Detection was conducted by a homebuilt Daly type detector, optimized for high m/z.

Author contributions

M.D. and B.J. designed the experiments, M.D. purified the proteins and performed all biochemical and ESR spectroscopy experiments and analyzed the data together with B.J. T.R. and N.M. performed and analyzed the LILBID-MS experiments. B.J. made the initial draft and finalized the manuscript together with all the authors. B.J. conceived the idea, acquired funding, supervised and administered the project.

Acknowledgements

This work was financially supported from the Deutsche Forschungsgemeinschaft via the Emmy Noether program (JO 1428/1−1), SFB 1507 − "Membrane-associated Protein Assemblies, Machineries, and Supercomplexes", and a large equipment fund (438280639) to B.J. N.M. acknowledges funding by the Deutsche Forschungsgemeinschaft (DFG, German Research Foundation) — Project-ID 426191805. B.J. and M.D. thanks Jingyi Liu for establishing $LptB_2FGC$ purification and PELDOR experiments.

Data Availability

The PELDOR/DEER data are available upon request to B.J.

For correspondence:

benesh.joseph@fu-berlin.de

References

1. Nikaido, H. Molecular basis of bacterial outer membrane permeability revisited. *Microbiol Mol Biol Rev* **67**, 593-656 (2003).
2. Whitfield, C. & Trent, M.S. Biosynthesis and export of bacterial lipopolysaccharides. *Annual Review of Biochemistry, Vol 85* **83**, 99-128 (2014).
3. Wu, T. et al. Identification of a protein complex that assembles lipopolysaccharide in the outer membrane of Escherichia coli. *Proc Natl Acad Sci USA* **103**, 11754-9 (2006).
4. Ruiz, N., Gronenberg, L.S., Kahne, D. & Silhavy, T.J. Identification of two inner-membrane proteins required for the transport of lipopolysaccharide to the outer membrane of Escherichia coli. *Proc Natl Acad Sci USA* **105**, 5537-42 (2008).

5. Chng, S.S., Gronenberg, L.S. & Kahne, D. Proteins required for lipopolysaccharide assembly in Escherichia coli form a transenvelope complex. *Biochemistry* **49**, 4565-7 (2010).
6. Lundstedt, E., Kahne, D. & Ruiz, N. Assembly and Maintenance of Lipids at the Bacterial Outer Membrane. *Chem Rev* (2020).
7. Sperandeo, P., Martorana, A.M. & Polissi, A. The Lpt ABC transporter for lipopolysaccharide export to the cell surface. *Res Microbiol* **170**, 366-373 (2019).
8. Ho, H. et al. Structural basis for dual-mode inhibition of the ABC transporter MsbA. *Nature* **557**, 196-201 (2018).
9. Vetterli, S.U. et al. Thanatin targets the intermembrane protein complex required for lipopolysaccharide transport in Escherichia coli. *Sci Adv* **4**, eaau2634 (2018).
10. Zampaloni, C. et al. A novel antibiotic class targeting the lipopolysaccharide transporter. *Nature* **625**, 566-571 (2024).
11. Pahil, K.S. et al. A new antibiotic traps lipopolysaccharide in its intermembrane transporter. *Nature* **625**, 572-577 (2024).
12. Mandler, M.D. et al. Novobiocin Enhances Polymyxin Activity by Stimulating Lipopolysaccharide Transport. *J Am Chem Soc* **140**, 6749-6753 (2018).
13. Martin-Loeches, I., Dale, G.E. & Torres, A. Murepavadin: a new antibiotic class in the pipeline. *Expert Rev Anti Infect Ther* **16**, 259-268 (2018).
14. Tork, L., Moffatt, C.B., Bernhardt, T.G., Garner, E.C. & Kahne, D. Single-molecule dynamics show a transient lipopolysaccharide transport bridge. *Nature* **623**, 814-819 (2023).
15. Narita, S. & Tokuda, H. Biochemical characterization of an ABC transporter LptBFGC complex required for the outer membrane sorting of lipopolysaccharides. *FEBS Lett* **583**, 2160-4 (2009).
16. Sperandeo, P. et al. Characterization of lptA and lptB, two essential genes implicated in lipopolysaccharide transport to the outer membrane of Escherichia coli. *J Bacteriol* **189**, 244-53 (2007).
17. Thomas, C. & Tampe, R. Structural and Mechanistic Principles of ABC Transporters. *Annu Rev Biochem* **89**, 605-636 (2020).
18. Wang, Z. et al. Structural and functional studies of conserved nucleotide-binding protein LptB in lipopolysaccharide transport. *Biochem Biophys Res Commun* **452**, 443-9 (2014).
19. Dong, H. et al. Structural basis for outer membrane lipopolysaccharide insertion. *Nature* **511**, 52-6 (2014).
20. Tang, X. et al. Cryo-EM structures of lipopolysaccharide transporter LptB2FGC in lipopolysaccharide or AMP-PNP-bound states reveal its transport mechanism. *Nat Commun* **10**, 4175 (2019).
21. Dong, H., Zhang, Z., Tang, X., Paterson, N.G. & Dong, C. Structural and functional insights into the lipopolysaccharide ABC transporter LptB2FG. *Nat Commun* **8**, 222 (2017).
22. Owens, T.W. et al. Structural basis of unidirectional export of lipopolysaccharide to the cell surface. *Nature* **567**, 550-553 (2019).
23. Li, Y., Orlando, B.J. & Liao, M. Structural basis of lipopolysaccharide extraction by the LptB2FGC complex. *Nature* **567**, 486-490 (2019).
24. Sherman, D.J. et al. Lipopolysaccharide is transported to the cell surface by a membrane-to-membrane protein bridge. *Science* **359**, 798-+ (2018).
25. Villa, R. et al. The Escherichia coli Lpt transenvelope protein complex for lipopolysaccharide export is assembled via conserved structurally homologous domains. *J Bacteriol* **195**, 1100-8 (2013).
26. Tran, A.X., Dong, C. & Whitfield, C. Structure and functional analysis of LptC, a conserved membrane protein involved in the lipopolysaccharide export pathway in Escherichia coli. *J Biol Chem* **285**, 33529-39 (2010).
27. Suits, M.D., Sperandeo, P., Deho, G., Polissi, A. & Jia, Z. Novel structure of the conserved gram-negative lipopolysaccharide transport protein A and mutagenesis analysis. *J Mol Biol* **380**, 476-88 (2008).
28. Okuda, S., Freinkman, E. & Kahne, D. Cytoplasmic ATP hydrolysis powers transport of lipopolysaccharide across the periplasm in E. coli. *Science* **338**, 1214-7 (2012).
29. Luo, Q. et al. Structural basis for lipopolysaccharide extraction by ABC transporter LptB2FG. *Nat Struct Mol Biol* **24**, 469-474 (2017).
30. Galazzo, L. & Bordignon, E. Electron paramagnetic resonance spectroscopy in structural-dynamic studies of large protein complexes. *Prog Nucl Magn Reson Spectrosc* 134-135, 1-19 (2023).
31. Tang, Q. et al. Asymmetric conformations and lipid interactions shape the ATP-coupled cycle of a heterodimeric ABC transporter. *Nat Commun* **14**, 7184 (2023).
32. Yardeni, E.H. et al. Probing the solution structure of the E. coli multidrug transporter MdfA using DEER distance measurements with nitroxide and Gd(III) spin labels. *Sci Rep* **9**, 12528 (2019).
33. Gopinath, A., Rath, T., Morgner, N. & Joseph, B. Lateral gating mechanism and plasticity of the beta-barrel assembly machinery complex in micelles and Escherichia coli. *PNAS Nexus* **3**, pgae019 (2024).
34. Sophie Ketter, M.D., Olga Rogozhnikova, Sergey A. Dobrynin, Victor M. Tormyshev, Elena G. Bagryanskaya, Benesh Joseph. In situ distance measurements in a membrane transporter using maleimide functionalized orthogonal spin labels and 5-pulse electron-electron double resonance spectroscopy. *J Magn Reson Open*, 100041 (2022).
35. Gopinath, A. & Joseph, B. Conformational Flexibility of the Protein Insertase BamA in the Native Asymmetric Bilayer Elucidated by ESR Spectroscopy. *Angew Chem Int Ed Engl* **61**, e202113448 (2022).
36. Kugele, A. et al. In situ EPR spectroscopy of a bacterial membrane transporter using an expanded genetic code. *Chem Commun (Camb)* **57**, 12980-12983 (2021).
37. Galazzo, L. et al. The ABC transporter MsbA adopts the wide inward-open conformation in E. coli cells. *Sci Adv* **8**, eabn6845 (2022).
38. Bountra, K. et al. Structural basis for antibacterial peptide self-immunity by the bacterial ABC transporter McjD. *EMBO J* **36**, 3062-3079 (2017).
39. Kapsalis, C. et al. Allosteric activation of an ion channel triggered by modification of mechanosensitive nano-pockets. *Nat Commun* **10**, 4619 (2019).
40. Ben-Ishay, Y. et al. Exploring the dynamics and structure of PpiB in living Escherichia coli cells using electron paramagnetic resonance spectroscopy. *Protein Sci* **33**, e4903 (2024).
41. Pierro, A. et al. In-cell investigation of the conformational landscape of the GTPase UreG by SDSL-EPR. *iScience* **26**, 107855 (2023).
42. Morgner, N. & Robinson, C.V. Massign: An Assignment Strategy for Maximizing Information from the Mass Spectra of Heterogeneous Protein Assemblies. *Anall Chem* **84**, 2939-2948 (2012).
43. Morgner, N., Barth, H.D. & Brutschy, B. A new way to detect noncovalently bonded complexes of biomolecules from liquid micro-droplets by laser mass spectrometry. *Aus J Chem* **59**, 109-114 (2006).
44. Pannier, M., Veit, S., Godt, A., Jeschke, G. & Spiess, H.W. Dead-time free measurement of dipole-dipole interactions between electron spins. *J Magn Reson* **142**, 331-40 (2000).
45. Schiemann, O. et al. Benchmark Test and Guidelines for DEER/PELDOR Experiments on Nitroxide-Labeled Biomolecules. *J Am Chem Soc* **143**, 17875-17890 (2021).
46. Grote, M. et al. Transmembrane Signaling in the Maltose ABC Transporter MalFGK(2)-E PERIPLASMIC MalF-P2 LOOP COMMUNICATES SUBSTRATE AVAILABILITY TO THE ATP-BOUND MalK DIMER. *J Biol Chem* **284**, 17521-17526 (2009).
47. Joseph, B., Jeschke, G., Goetz, B.A., Locher, K.P. & Bordignon, E. Transmembrane gate movements in the type II ATP-binding cassette (ABC) importer BtuCD-F during nucleotide cycle. *J Biol Chem* **286**, 41008-17 (2011).
48. Barth, K. et al. Conformational coupling and trans-inhibition in the human antigen transporter ortholog TmrAB resolved with dipolar EPR spectroscopy. *J Am Chem Soc* (2018).

49. Verhalen, B. et al. Energy transduction and alternating access of the mammalian ABC transporter P-glycoprotein. *Nature* **543**, 738-741 (2017).
50. Borbat, P.P. et al. Conformational motion of the ABC transporter MsbA induced by ATP hydrolysis. *PLoS Biol* **5**, e271 (2007).
51. Hutter, C.A.J. et al. The extracellular gate shapes the energy profile of an ABC exporter. *Nat Commun* **10**, 2260 (2019).
52. Majsnerowska, M. et al. Substrate-induced conformational changes in the S-component ThiT from an energy coupling factor transporter. *Structure* **21**, 861-7 (2013).
53. Hubbell, W.L., Gross, A., Langen, R. & Lietzow, M.A. Recent advances in site-directed spin labeling of proteins. *Curr Opin Struct Biol* **8**, 649-56 (1998).
54. Fabregas Ibanez, L., Jeschke, G. & Stoll, S. DeerLab: a comprehensive software package for analyzing dipolar electron paramagnetic resonance spectroscopy data. *Magn Reson (Gott)* **1**, 209-224 (2020).
55. Worswick, S.G., Spencer, J.A., Jeschke, G. & Kuprov, I. Deep neural network processing of DEER data. *Sci Adv* **4**, eaat5218 (2018).
56. Nicholas P. Cina, C.S.K. Conformational Investigation of the Asymmetric Periplasmic Domains of E. coli LptB2FGC Using SDSL CW EPR Spectroscopy. *Appl Magn Reson* **55**(2023).
57. Falchi, F.A. et al. Suppressor Mutations in LptF Bypass Essentiality of LptC by Forming a Six-Protein Transenvelope Bridge That Efficiently Transports Lipopolysaccharide. *mBio* **14**, e0220222 (2023).
58. Wilson, A. & Ruiz, N. The transmembrane alpha-helix of LptC participates in LPS extraction by the LptB(2) FGC transporter. *Mol Microbiol* **118**, 61-76 (2022).
59. Luo, Q., Shi, H. & Xu, X. Cryo-EM structures of LptB(2)FG and LptB(2)FGC from Klebsiella pneumoniae in complex with lipopolysaccharide. *Biochem Biophys Res Commun* **571**, 20-25 (2021).
60. Okuda, S., Sherman, D.J., Silhavy, T.J., Ruiz, N. & Kahne, D. Lipopolysaccharide transport and assembly at the outer membrane: the PEZ model. *Nat Rev Microbiology* **14**, 337-45 (2016).
61. Morbach, S., Tebbe, S. & Schneider, E. The ATP-binding cassette (ABC) transporter for maltose/maltodextrins of Salmonella typhimurium. Characterization of the ATPase activity associated with the purified MalK subunit. *J Biol Chem* **268**, 18617-21 (1993).
62. Tait, C.E. & Stoll, S. Coherent pump pulses in Double Electron Electron Resonance spectroscopy. *Physical Chemistry Chemical Physics* **18**, 18470-18485 (2016).
63. Teucher, M. & Bordignon, E. Improved signal fidelity in 4-pulse DEER with Gaussian pulses. *J Mag Reson* **296**, 103-111 (2018).
64. Jeschke, G. MMM: Integrative ensemble modeling and ensemble analysis. *Protein Sci* **30**, 125-135 (2021).

Supporting Information for

Dynamic basis of lipopolysaccharide export by $LptB_2FGC$

Marina Dajka[1], Tobias Rath[2], Nina Morgner[2], & Benesh Joseph[1*]

[1]Department of Physics, Freie Universität Berlin, Arnimallee 14, 14195, Germany

[2]Institute of Physical and Theoretical Chemistry, Goethe Universität Frankfurt, Max-von Laue Strasse 9, 60438, Germany

[*]Corresponding author: benesh.joseph@fu-berlin.de

Supplementary Figures

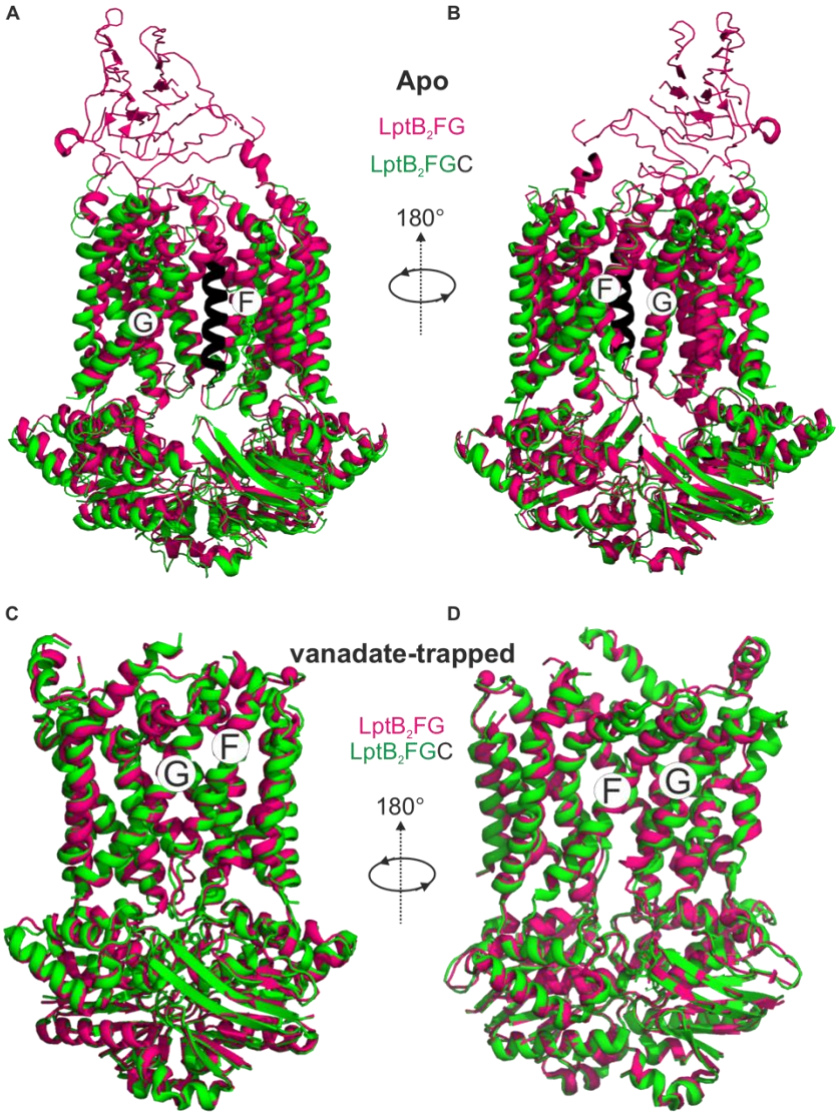

Figure S1. LptB$_2$FG and LptB$_2$FGC structures in the apo and vanadate-trapped states. (A) *E. coli* LptB$_2$FG (magenta, PDB ID: 6MHU) and LptB$_2$FGC (LptB$_2$FG subunits in green and LptC in black, PDB ID: 6MI7) structures in the apo state are overlaid. The gating helices named as G and F moves apart upon binding LptC. A view from the other lateral gate is shown in (B). (C) *E. coli* LptB$_2$FG (magenta, PDB ID: 6MHZ) and LptB$_2$FGC (PDB ID: 6MI8) structures in the vanadate-trapped states are overlaid. The TM-LptC is not resolved in LptB$_2$FGC and the structures are nearly identical with an overall RMDS of 0.99 Å.

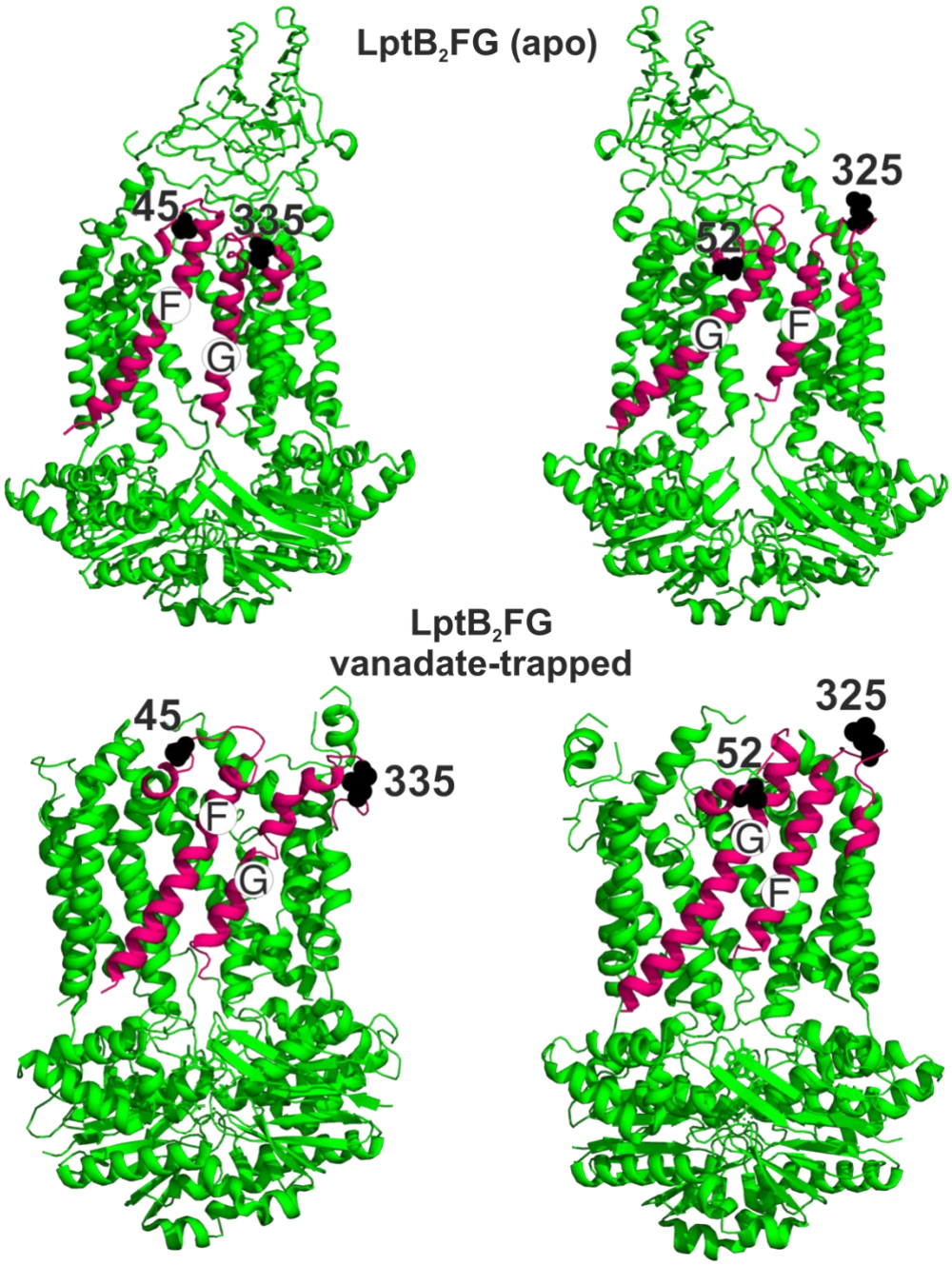

Figure S2. Spin labeled positions in $LptB_2FG$. The two lateral gates (magenta) and the labeled positions (black spheres) are highlighted on the apo (PDB ID: 6MHU) and vanadate-trapped (PDB ID: 6MHZ) $LptB_2FG$ structures (top and bottom, respectively).

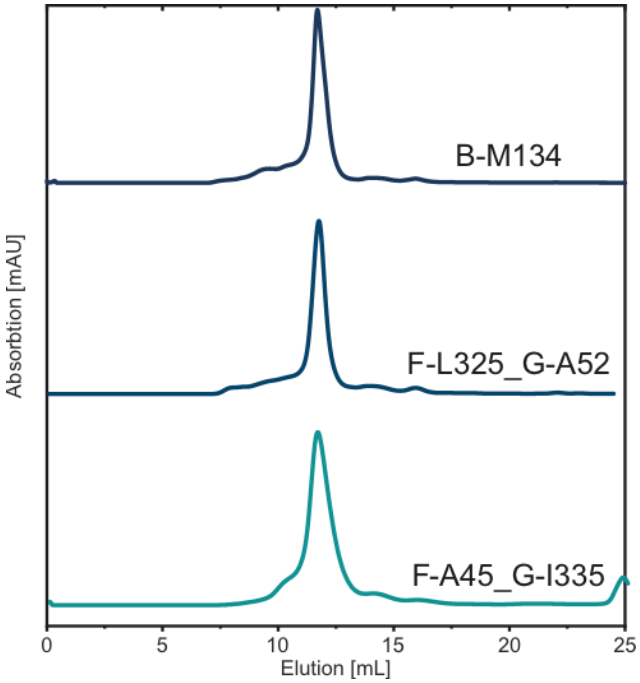

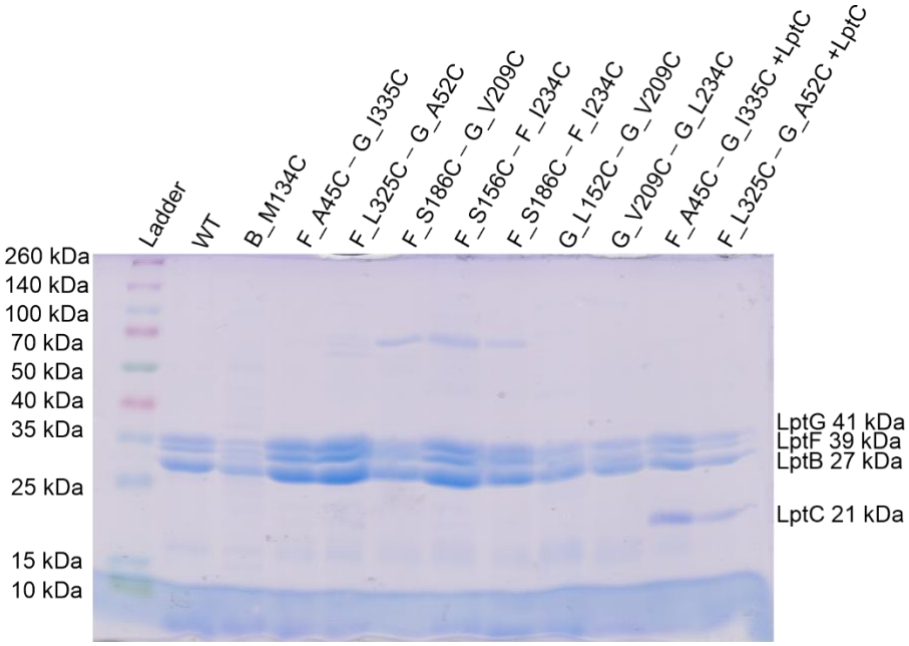

Figure S3. Size-exclusion chromatography (SEC) and SDS-PAGE for WT and spin labeled cysteine variants of $LptB_2FG$ and $LptB_2FGC$. (Top panel) Typical SEC profiles for selected spin labeled variants as indicated are shown. (Bottom panel) SDS-PAGE gel. Proteins were collected from SEC column and the molecular weight of the subunits are indicated (LptG 41 kDa, LptF 39 kDa, LptB 27 kDa and LptC 21 kDa).

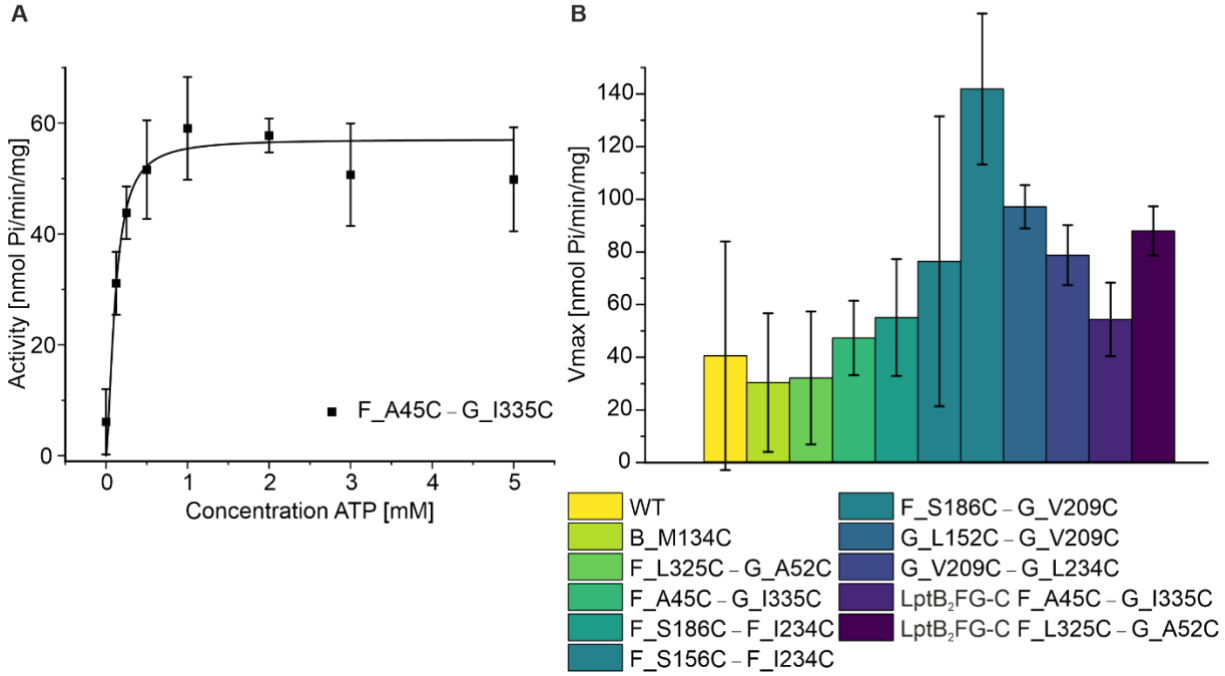

Figure S4. ATPase assay for spin labeled variants of $LptB_2Fg$ and $LptB_2FGC$. The functionality of the spin labelled proteins were characterized using ATPase assay and typical reaction curve is shown (left). The corresponding V_{max} values are shown (right). All the variants actively hydrolysed ATP, in line with the conformational changes observed from PELDOR/DEER experiments following vanadate-trapping (Figures 2-6). As the variants are spin labelled at different positions, a quantitative comparison between the values is omitted.

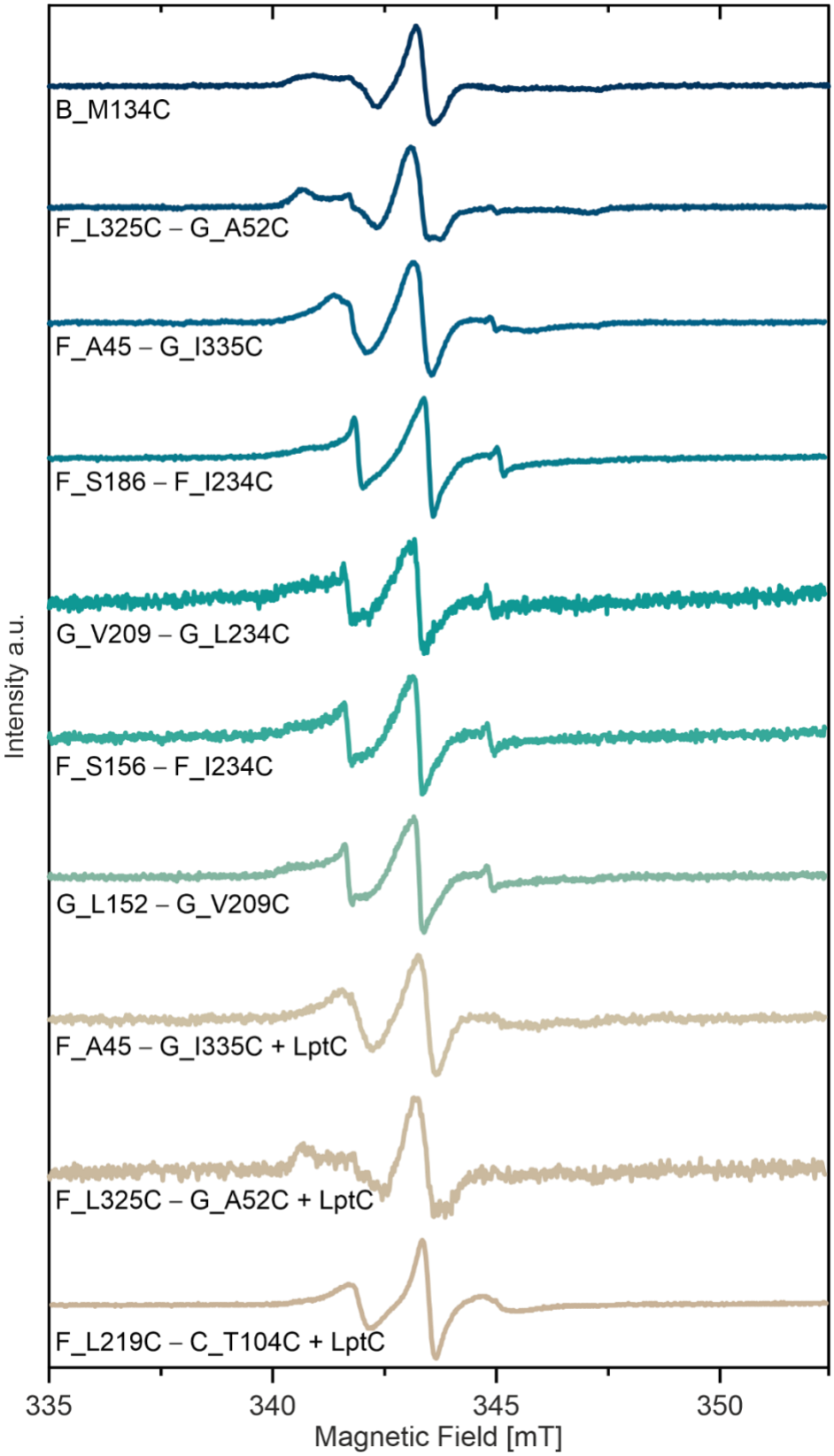

Figure S5. Room temperature continuous wave ESR spectroscopy of MTSL labeled variants in micelles. Spectra for spin labelled $LptB_2FG$ and $LptB_2FG$-C variants in DDM micelles are shown.

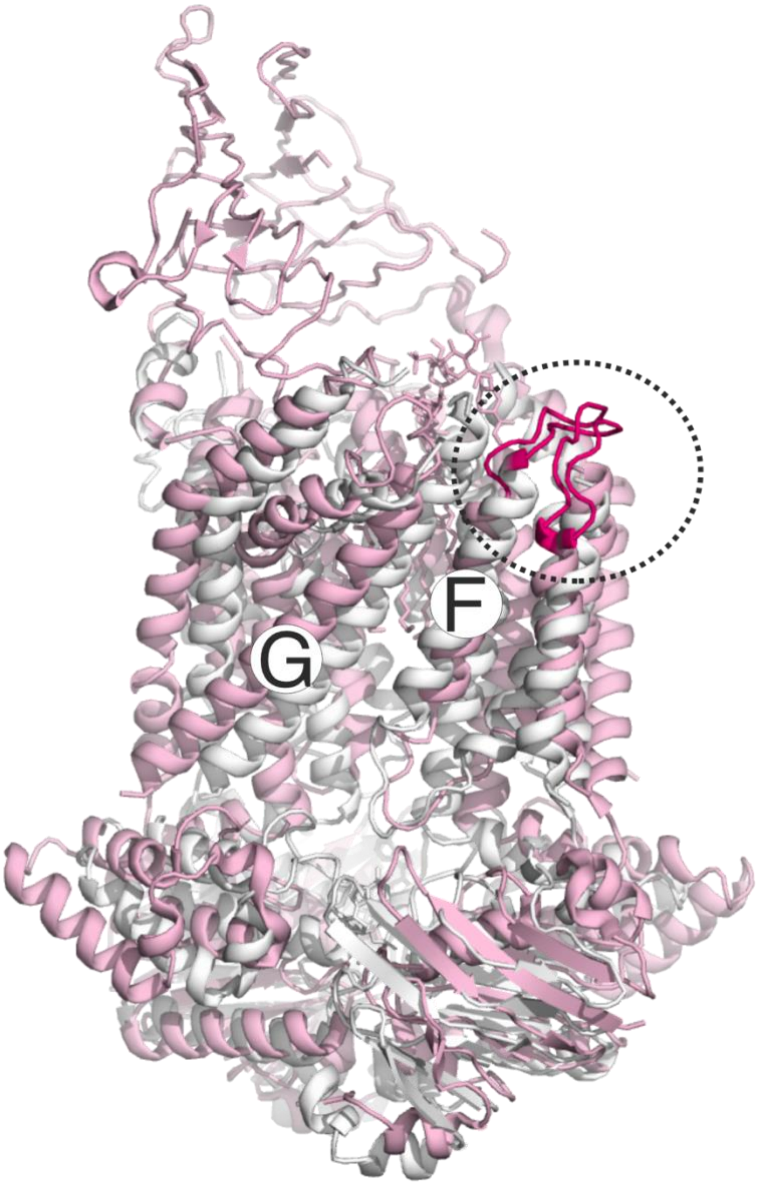

Figure S6. Conformation of the loop carrying the spin labeled position 325 in LptF at the second lateral gate. $LptB_2FG$ apo (pink, PDB ID: 6MHU) and vanadate-trapped (grey, PDB ID: 6MHZ) structures are overlaid. The loop carrying the spin labelled position L325 is highlighted (magenta), which has a rather similar conformation in the two structures.

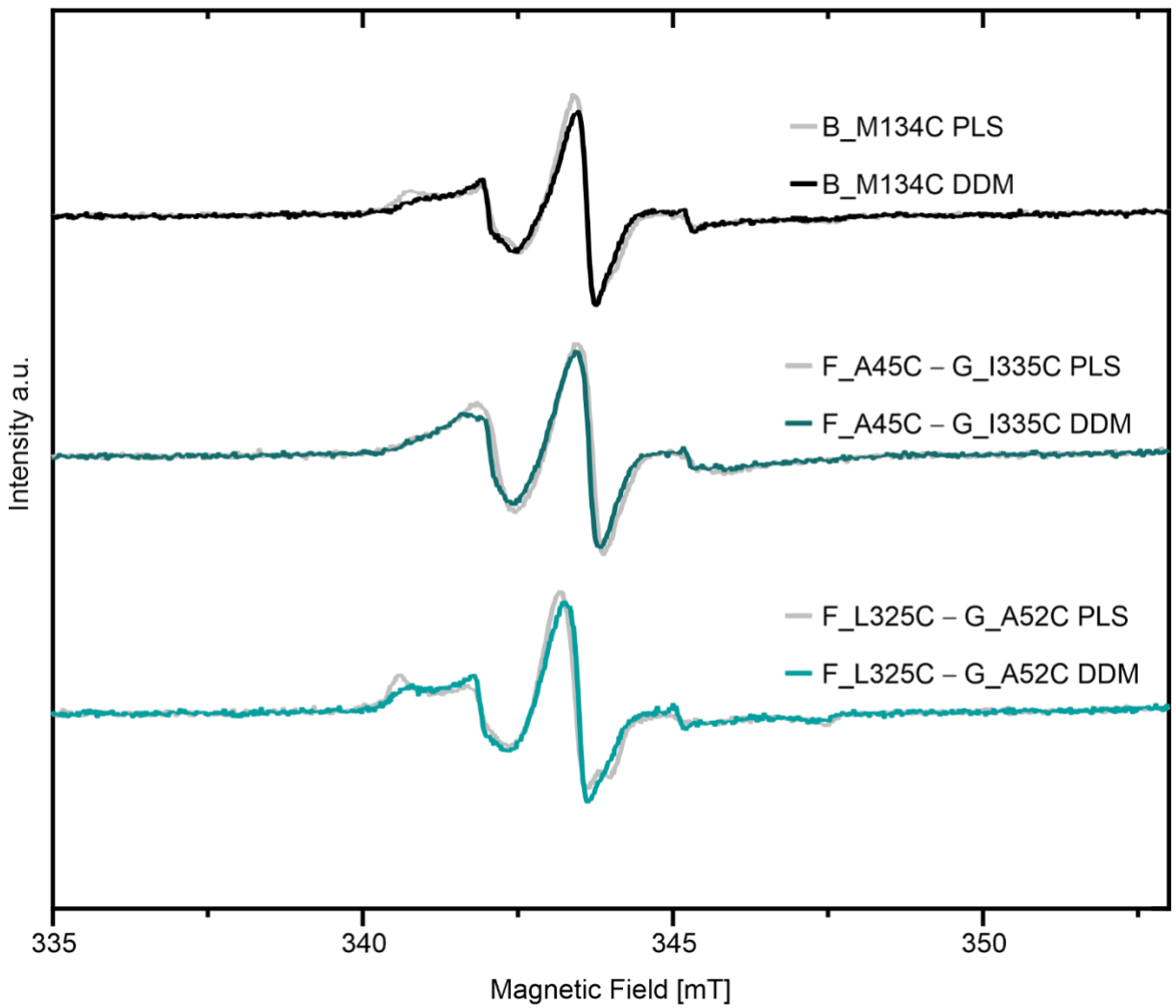

Figure S7. Comparison of room temperature continuous wave ESR spectroscopy of MTSL labeled variants between DDM micelles and proteoliposomes (PLS). Corresponding spectra for spin labelled $LptB_2FG$ variants in liposomes and DDM micelles are shown.

Variant	Protein [μM] (±10%)	Spin [μM] (±10%)	Labelling efficiency [%] (±15%)
B_M134C PLS	60	125	96
F_A45C – G_I335C	37	72	98
F_L325C – G_A52C	37	69	93
F_S186C – G_V209C	31	70	112
F_S156C – F_I234C	70	130	93
F_S186C – F_I234C	31	61	99
G_L152C – G_V209C	46	87	95
G_V209C – G_L234C	34	64	94
F_A45C – G_I335C + LptC	29	58	100
F_L325C – G_A52C + LptC	31	62	100

Table S1. Spin labelling efficiency for the investigated cysteine variants. A 10% error is estimated for the protein and spin concentrations.